Journal of Materials Chemistry A

COMMUNICATION

View Article Online
View Journal | View Issue

Cite this: J. Mater. Chem. A, 2018, 6, 21280

Received 12th September 2018
Accepted 12th October 2018

DOI: 10.1039/c8ta08875f

rsc.li/materials-a

An ordered mesoporous silica framework based electrolyte with nanowetted interfaces for solid-state lithium batteries†

Lei Han, Ziqi Wang, * Defei Kong, Luyi Yang, Kai Yang, Zijian Wang and Feng Pan *

The practical applications of lithium metal as an anode material are hindered by the uncontrollable growth of lithium dendrites. Herein, an ordered mesoporous silica framework (MCM-41) based solid-state electrolyte (Li-IL@MCM-41 SSE) with nanoconfined ionic liquids is prepared through a post-impregnation method. The as-prepared electrolyte with nanowetted interfaces demonstrates suppression towards lithium dendrites, high thermal stability (up to 350 °C) and excellent electrochemical properties, such as high ionic conductivity (3.98×10^{-4} S cm^{-1} at 30 °C), a broad electrochemical potential window (up to 5.2 V) and good compatibility with different electroactive materials. The solid-state batteries (SSBs) assembled exhibited excellent cycling performance, delivering capacities of 138 mA h g^{-1}, 127 mA h g^{-1} and 163 mA h g^{-1} after 100 cycles at room temperature with $LiFePO_4$, $LiCoO_2$, and $LiNi_{0.8}Co_{0.1}Mn_{0.1}O_2$ cathode materials, respectively. The good battery performance can be ascribed to the effective three-dimensional ion-conducting networks established by the nanowetted interfaces. The aforementioned results exhibit the good prospects of the Li-IL@MCM-41 SSE for application in lithium metal batteries.

Introduction

The growing demand for portable electronic devices, electric vehicles and grid-scale energy storage has stimulated intensive research on lithium-ion batteries with better safety and higher energy density.[1] The conventional carbon anode, primarily based on graphite, is limited by its relatively low theoretical capacity of 370 mA h g^{-1}. Lithium (Li) metal is an ideal anode material for next generation rechargeable batteries, because it has the highest specific capacity of 3860 mA h g^{-1} and the lowest negative electrochemical potential of −3.04 V *vs.* the standard hydrogen electrode.[2] Unfortunately, the practical applications of Li metal batteries are hindered by the growth of Li dendrites and the low coulombic efficiency during the charge/discharge process.[3] Conventional organic liquid electrolytes would react with Li to form an inhomogeneous and mechanically fragile solid electrolyte interphase (SEI) layer on the Li anode, resulting in the formation of Li dendrites that can induce short circuits and accompanying safety hazards.[4]

Solid-state electrolytes (SSEs) are currently widely investigated as a potential solution to solve the challenges encountered in Li metal batteries due to their inherent advantage in mechanical strength, safety and device fabrication. Generally, high ionic conductivity, a broad electrochemical window and good electrolyte/electrode interfacial compatibility are required for SSEs to provide good battery performance. However, until now, very few solid-state electrolytes with a combination of the aforementioned properties have been found. Polymer based solid electrolytes can only operate in a narrow temperature range due to their low room-temperature ionic conductivity and poor thermal stability, and their electrochemical window is also limited.[5,6] Inorganic solid electrolytes have long been suffering from an unstable electrolyte/electrode interface contact with large interfacial and grain boundary resistance, because of their rigid nature.[7–9] Besides, some composite electrolytes have also been designed recently towards high power and safety, such as Li_3OCl coated ceramic solid electrolyte,[9] and zeolite[10] and ceramic[11] doped polymer electrolytes.

Novel SSEs with "nanowetted interfaces" and high mechanical robustness can be prepared by impregnating ion-conducting guests into inert porous solid hosts.[12,13] Li^+ containing ionic liquids (Li-IL) are ideal conducting guests offering high ionic conductivity with stable electrochemical performance owing to their attractive properties, including non-flammability, negligible vapour pressure, excellent thermal stability and a wide electrochemical window.[14] The porous solid hosts act as the scaffolds in SSEs, which prevent the conducting guests from leakage and provide sufficient mechanical strength to suppress Li dendrite growth. Our previous work[15,16]

School of Advanced Materials, Peking University Shenzhen Graduate School, Shenzhen 518055, China. E-mail: wangzq@pkusz.edu.cn; panfeng@pkusz.edu.cn

† Electronic supplementary information (ESI) available: N_2 adsorption/desorption isotherms, t_{Li^+} of pristine Li-IL, TGA, SEM for Li metal after cycling, double-layered pellets and XPS. See DOI: 10.1039/c8ta08875f

demonstrated an SSE designed using Li-IL impregnated MOF nanocrystals to generate nanowetted interfaces. The unique interfaces enable an interfacial wettability effect of the nano-confined Li-IL guests which can directly come into contact with the surfaces of cathode particles and the Li metal anode. The solid–solid contact in conventional SSBs is avoided by such a nanowetted interfacial mechanism to reduce the interfacial ion transport resistance. Despite the good electrochemical properties, the cost of MOFs is too high for practical applications and the electrochemical window of the SSE is limited by the organic ligands and the redox-active metal centres. To design SSEs with nanowetted interfaces and good electrochemical performance for practical usage, in this work, we utilized MCM-41,[17] a typical silica with well-ordered 2D hexagonal arrays of mesoporous channels, as the nanoporous scaffold due to its high porosity, sufficient mechanical robustness and excellent electrochemical stability. And we chose Pyr14TFSI as the ion conductive guest due to its wide electrochemical window, relatively high ionic conductivity, high thermal stability and non-flammability.[18–20] The Li salt concentration was set at 0.5 M to strike a balance between the Li^+ transference number and ionic conductivity.[18–22] The Li-IL@MCM-41 SSE was prepared by the confinement of Li-IL within nanoporous MCM-41 nanoparticles *via* a post-impregnation method, revealing high ionic conductivity, a broad electrochemical window and the capability of suppressing Li dendrites. It also demonstrated good compatibility with different cathode materials, such as $LiFePO_4$, $LiCoO_2$, and $LiNi_{0.8}Co_{0.1}Mn_{0.1}O_2$, and the solid-state batteries (SSBs) assembled delivered excellent cycling performance.

Experimental

Synthesis of MCM-41 nanoparticles

Firstly, 0.94 g cetyltrimethylammonium bromide (CTAB) was dissolved in 480 mL deionized water. Then 3.5 mL NaOH aqueous solution (2.0 mol L^{-1}) was added to the CTAB solution. 5.5 mL tetraethyl orthosilicate (TEOS) was added dropwise to the CTAB solution. The reaction mixture was subsequently stirred at 70 °C for 3 h to give rise to white precipitates. The precipitated product was filtered, washed with deionized water and methanol, and dried at 80 °C for 2 days. The dry precipitates (1.4 g) were refluxed in a mixed solution of 120 mL 1,4-dioxane, 34 mL deionized water and 8 mL concentrated HCl at 105 °C for one day. The product was filtered, washed with deionized water and methanol, and dried at 80 °C for 2 days to obtain the ordered mesoporous silica, MCM-41 nanoparticles. The MCM-41 nanoparticles were activated at 150 °C in a vacuum and stored in an Ar glovebox for further use.

Preparation of Li-IL@MCM-41 and a solid-state composite cathode

287 mg (1 mmol) bis(trifluoromethane)sulfonimide lithium (LiTFSI) was dissolved in 2 mL *N*-butyl-*N*-methylpyrrolidinium bis(trifluoromethane)sulfonimide (Pyr14TFSI) obtaining a Li^+ containing ionic liquid (Li-IL). Different amounts of Li-IL were added to the MCM-41 nanoparticles, milled into homogeneous mixtures in an Ar glovebox and heated at 150 °C in a vacuum for 4 hours to obtain the "free-flowing" Li-IL@MCM-41 SSE powder.

Different types of commercial electroactive materials ($LiNi_{0.8}Co_{0.1}Mn_{0.1}O_2$, Shenzhen Optimumnano Energy Co., Ltd, China; $LiCoO_2$, Tianjin B&M Science and Technology Joint-Stock Co., Ltd, China; $LiFePO_4$, Shenzhen Dynanonic Co., Ltd, China), Li-IL@MCM-41 and acetylene black were milled into homogeneous mixtures respectively in an Ar glovebox in a mass ratio of 5 : 5 : 2 to obtain the solid-state composite cathode powder.

Characterization

The morphological and elemental mapping studies were performed by FEITecnaiG230 transmission electron microscopy (TEM) and ZEISS Supra 55 scanning electron microscopy (SEM) with an Oxford AZtec energy dispersive spectrometer. Powder X-ray diffraction (XRD) data were recorded by using a Bruker D8 Advance diffractometer using Cu Kα ($\lambda = 1.541$ Å) from 1 to 15°. N_2 adsorption/desorption isotherms were recorded on a Micromeritics ASAP 2020 HD88 tool. The surface area was calculated using the Brunauer–Emmett–Teller (BET) model and a density functional theory (DFT) model based on the nitrogen adsorption data derived pore size distribution. Thermogravimetric analysis was performed on a Mettler Toledo TGA/DSC STAR system at a heating rate of 10 °C min^{-1} under N_2 flow. The cyclic voltammetry (CV, 0.2 mV s^{-1}), linear sweep voltammetry (LSV, 0.2 mV s^{-1}) and electrochemical impedance spectroscopy (EIS, 1–10^6 Hz) data were collected on a CHI600E electrochemical workstation. The Li plating/stripping cycles, battery rate performance and battery cycling behaviour were investigated with a NEWARE battery cycler. The X-ray photoelectron spectra (XPS) of the Li metal surface were acquired on a Thermo Fisher ESCALAB 250X surface analysis system with a monochromatized Al anode X-ray source, and an argon ion beam (accelerating voltage 3 kV) was employed to perform depth profiling (etching area, 1 × 1 mm^2). An argon atmosphere controlled glove bag was employed to transfer the sample from the glove box to the XPS system.

Electrochemical measurements

In an Ar glovebox, 60 mg Li-IL@MCM-41 was pressed into a 12 mm pellet under 8 t force and assembled into CR2025 coin cells for the ionic conductivity (SS|Li-IL@MCM-41|SS), electrochemical window (SS|Li-IL@MCM-41|Li), Li transference number (Li|Li-IL@MCM-41|Li) and Li plating/stripping (Li|Li-IL@MCM-41|Li) tests. The Li transference number test for the pristine Li-IL was similar, but a Whatman glass fibre filter was used as the separator. For battery assembly, 2.2 mg composite cathode powder was added into a 7 mm mould and pressed into a pellet under 1 t force. The cathode pellet was then put in the centre of a 12 mm mould and 45 mg Li-IL@MCM-41 was added subsequently, which were further pressed into a 12 mm bilayer pellet under 8 t force. Solid-state batteries (Scheme 1) were assembled and tested in CR2025 coin cells using Li foil (about

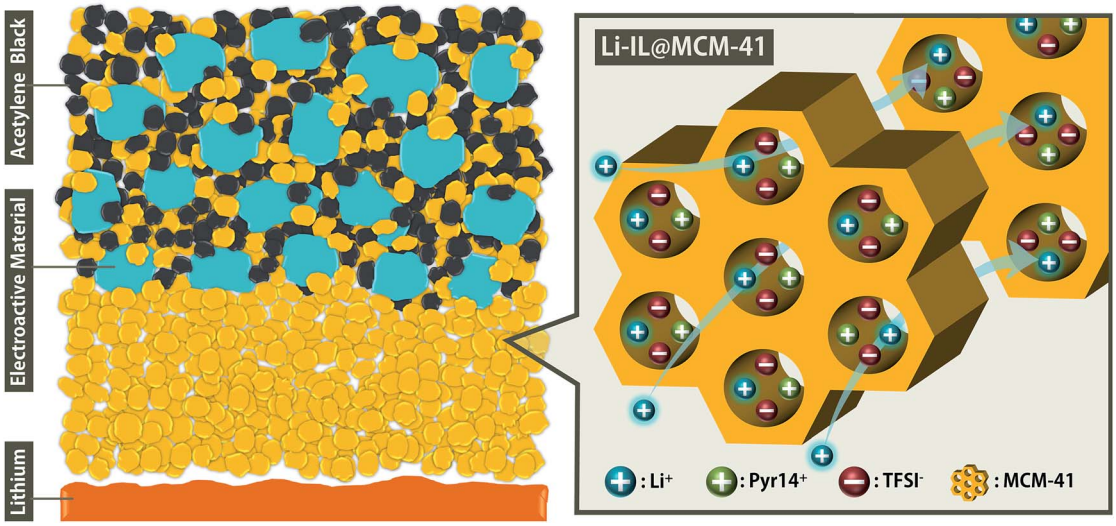

Scheme 1 Left: schematic illustration of the battery architecture composed of a double-layered pellet and lithium foil. Right: ion-conducting mechanism of the Li-IL@MCM-41 SSE.

1 mm thick) as the anode and the bilayer pellet as the cathode and electrolyte.

Results and discussion

The as-synthesized MCM-41 nanoparticles were nearly spherical with a diameter of about 70 nm, as indicated by the SEM morphology in Fig. 1b. The N_2 adsorption/desorption isotherm of MCM-41 is illustrated in Fig. S1.† It shows type IV isotherms of typical mesoporous materials,[23] with a total pore volume of 1.17 $cm^3\ g^{-1}$ and a BET surface area of 925 $m^2\ g^{-1}$. The well-ordered mesoporous structure of MCM-41 was confirmed by the TEM images in Fig. 1a, and the average pore size was about 3 nm, which was consistent with the BJH pore size distribution plot in the inset of Fig. S1.† The porous structure of MCM-41 which demonstrates a 2D hexagonal (*P6mm*) structure was maintained after being pressed under 8 t force as proved by its XRD shown in Fig. S2.†[24] As analysed above, the mechanically stable and highly porous MCM-41 nanoparticles with well-ordered arrays of mesoporous channels were successfully obtained.

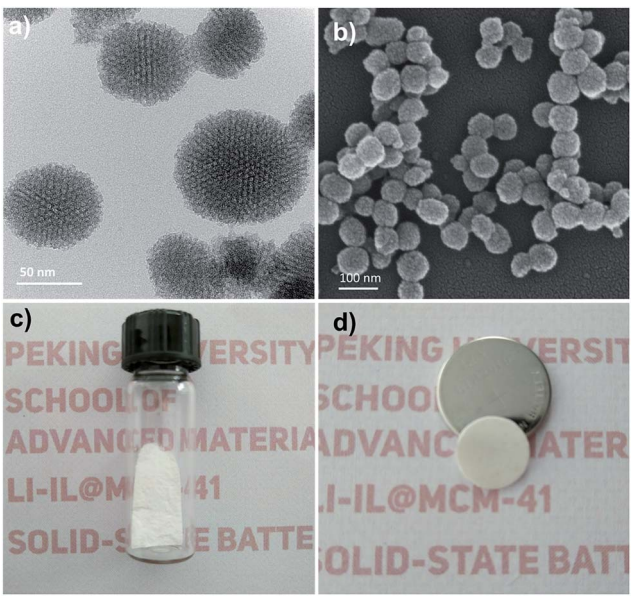

Fig. 1 (a) TEM and (b) SEM images of the nanosized MCM-41. Photographs of (c) the free-flowing Li-IL@MCM-41 powder and (d) the Li-IL@MCM-41 SSE pellet.

Ionic conductivity is one of the most significant performance parameters of a solid-state electrolyte for electrochemical applications. The occupancy rate of Li-IL in Li-IL@MCM-41 directly determines its ionic conductivity.[25] In order to maximize the Li-IL loading and thus achieve a higher ionic conductivity, the content of Li-IL in the Li-IL@MCM-41 composite was first optimized before other tests. The MCM-41 nanoparticles were activated at 150 °C in a vacuum before use to remove trace water inside the pores. Different amounts of Li-IL were milled with the activated MCM-41 nanoparticles in an Ar glovebox and heated at high temperature under vacuum for several hours. Through this process, the residual guest molecules, such as Ar molecules, inside the pores of MCM-41 were evacuated from the pores and the viscosity of Li-IL was reduced for better impregnation. The as-prepared nanocomposites appeared to be a "free-flowing" dry powder as shown in Fig. 1c, which was directly pressed into self-standing pellets (Fig. 1d) afterward for ionic conductivity determination by EIS using silver-coated stainless steel (SS) electrodes at temperatures ranging from 30 to 100 °C. Fig. 2a shows the Arrhenius relationship between ionic conductivity and temperature for the Li-IL@MCM-41 pellets with different Li-IL contents. As expected, the highest ionic conductivity of Li-IL@MCM-41 was obtained when the occupancy rate was highest at 2.2 mL@1 g. The ionic conductivity of this sample is 3.98×10^{-4} S cm^{-1} at 30 °C, 1.26×10^{-3} S cm^{-1} at 60 °C, and 2.51×10^{-3} S cm^{-1} at 100 °C. The ionic conduction of intra-particles should be ascribed to

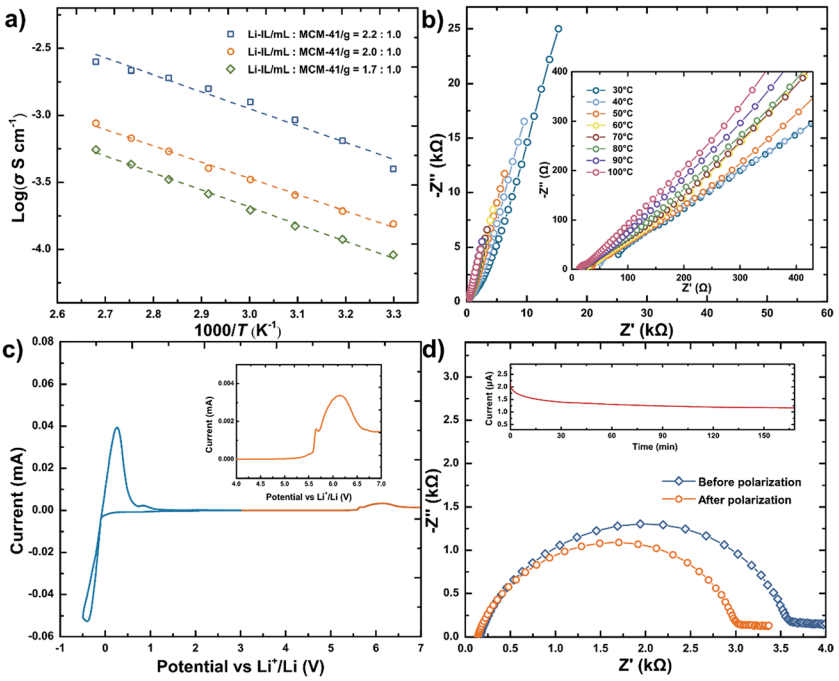

Fig. 2 (a) Arrhenius plots for the ionic conductivity of Li-IL@MCM-41 with different Li-IL occupancy rates. (b) EIS of Li-IL@MCM-41 (2.2 mL@1 g) at temperatures ranging from 30 to 100 °C. (c) CV (−0.5 to 3 V) and LSV (3 to 7 V) profiles of the SS|Li-IL@MCM-41|Li asymmetric cell at room temperature. Inset: magnified region of 4–7 V. (d) EIS of the Li|Li-IL@MCM-41 (2.2 mL@1 g)|Li symmetric cell before and after the DC polarization at room temperature. Inset: time-dependent current response of DC polarization for the symmetric cell.

the nanoconfined Li-IL within the pores. In contrast to conventional ceramic SSEs, which suffer from large interfacial resistance originating from the solid–solid contact, the ionic conduction of inter-particles is facilitated by the abundant nanowetted interfaces. The composite with more Li-IL felt like a wet gel, indicating that the MCM-41 scaffold could not confine more Li-IL. EIS (Fig. 2b) of the SS|Li-IL@MCM-41|SS cell shows a typical Nyquist plot with a straight tail at each testing temperature, showing that it maintains the ion conducting features of a liquid electrolyte while exhibiting a solid state. The activation energies of Li-IL@MCM-41 were calculated according to the Arrhenius equation:

$$\sigma_{DC} = \sigma_{\infty} \exp\left(-\frac{E_a}{RT}\right)$$

σ_{DC}, σ_{∞} and E_a are the conductivity at the corresponding temperature, the conductivity at infinite temperature and the activation energy for ionic conduction, respectively. The E_a of Li-IL@MCM-41 with occupancy rates of 2.2, 2.0 and 1.7 mL@1 g is 24.1, 23.3 and 24.4 kJ mol^{-1}, respectively. The samples exhibit higher energy barriers for ionic transport than pure ionic liquid,[18] which should be attributed to the interaction between the guest ions and the porous host. Another important parameter that must be considered for Li metal battery applications is the electrochemical stability, which was investigated by linear sweep voltammetry (LSV) and cyclic voltammetry (CV) tests at room temperature. As illustrated in the inset of Fig. 1c, Li-IL@MCM-41 exhibited anodic stability up to 5.2 V *versus* Li$^+$/Li, which indicates its potential application in high-voltage cathodes. The significant current peaks at ∼−0.3 V and +0.3 V were observed in cyclic voltammetry corresponding to the deposition and stripping of the lithium ion on the stainless steel.[26] As shown in Fig. 1c, the cathodic limiting potential of Li-IL@MCM-41 was about 0 V, and the electrochemical potential window was thus calculated to be 5.2 V. The broad electrochemical window indicates excellent electrochemical stability of the Li-IL@MCM-41 SSE for Li metal battery applications.

The lithium-ion transference number (t_{Li^+}) of Li-IL@MCM-41 was measured *via* the steady-state current method proposed by Bruce and Vincent.[27] A Li|Li-IL@MCM-41|Li symmetrical cell was assembled and 10 mV direct current (DC) potential was applied to the cell. The time-dependent current response of DC polarization and the EIS of the cell before and after polarization are shown in Fig. 1d. The lithium-ion transference number was calculated by using the following equation:

$$t_{Li^+} = \frac{I_s(\Delta V - I_0 R_0)}{I_0(\Delta V - I_s R_s)}$$

wherein ΔV is the applied DC potential, I is the current, R refers to the interface resistance, and 0 and s represent the initial and steady states, respectively. The t_{Li^+} values of Li-IL@MCM-41 with occupancy rates at 2.2, 2.0 and 1.7 mL@1 g were calculated to be 0.17 (Fig. 1d), 0.13 (Fig. S3a†) and 0.12 (Fig. S3b†), respectively. And the value of pristine Li-IL, measured by the same method, was calculated to be 0.09 (Fig. S3c†). The enhancement of the transference number is

probably due to the preferential interaction between the anions of IL and the silanol groups on the pore surfaces with a Lewis acid characteristic and the relatively limited movement of organic ions that possess a larger diameter than Li ions.[28]

The thermal stabilities of pristine MCM-41, pristine Li-IL and Li-IL@MCM-41 were revealed by TGA. For Li-IL and Li-IL@MCM-41, a monotonic decrease around 360 °C in weight was observed (Fig. S4†), while the weight of pristine MCM-41 nearly stayed unchanged from 25 to 700 °C. The curves of pristine Li-IL and Li-IL@MCM-41 were almost identical, except that the residual weight of Li-IL@MCM-41 at 700 °C was higher than that of pristine Li-IL. This means that the thermal stability of Li-IL@MCM-41 is primarily determined by Li-IL and has little relationship with the scaffold MCM-41. The thermal decomposition temperature of above 350 °C demonstrates the favourable thermal stability of Li-IL@MCM-41.

To assess the long-term stability and Li-ion transport capability of the interfaces between Li-IL@MCM-41 and Li metal, the DC Li plating/stripping experiment was carried out using a Li|Li-IL@MCM-41|Li symmetrical cell. Fig. 3a shows the time-dependent voltage profile of the cell at a current density of 0.025 mA cm^{-2} at room temperature (10 hours for each cycle), and the polarization voltage is around 0.1 V. Higher current densities of 0.10, 0.15 and 0.20 mA cm^{-2} were also examined on the symmetrical cells, and the polarization voltages increased to about 0.2, 0.3 and 0.6 V, respectively, as shown in Fig. S5.† During repeated Li plating/stripping cycling, the polarization voltage showed a negligible fluctuation after the first few cycles and remained stable over 1000 h without a short circuit as shown in Fig. 3a. This indicates a stable interface between Li-IL@MCM-41 and Li metal during cycling. EIS Nyquist plots of the Li|Li-IL@MCM-41|Li cell before and after Li plating/stripping cycles were recorded, as shown in Fig. 3b. The total resistance of the cell decreased from 2924 Ω to 1219 Ω after cycling, and the polarization voltage decreased from 200 mV in the first cycle to 90 mV. Li dendrites formed in the conventional liquid electrolyte hinder the practical application of the Li metal anode. The high Li^+ conduction pathways of an inhomogeneous SEI provide Li nucleation sites. The Li nuclei uncontrollably grow by fracturing the fragile SEI around them and self-ramify to form dendritic structures as illustrated in the upper panel of Fig. 3d.[3,4] Eventually, the Li dendrites will penetrate the separator with weak mechanical strength and lead to battery failure. To investigate the difference of Li deposition in the Li-IL@MCM-41 SSE, the cycled symmetric cells were disassembled and studied by SEM. The surface of Li metal revealed a smooth and dense morphology after plating/stripping cycles (Fig. S6†). Strong mechanical strength and plentiful nanowetted interfaces provided by the Li-IL@MCM-41 SSE favoured the uniform deposition of Li. Fig. 3c shows an enlarged region of Li metal after cycling, where some nanostructures were exposed after several minutes of electron bombardment. Instead of Li dendrites, many flake-shaped structures with nanoscale thickness can be observed. Instead of dendritic deposition, Li tended to deposit in a flaky form in the cells under the suppression of Li-IL@MCM-41, as illustrated in the lower panel of Fig. 3d. And the potential penetration will be stopped by the firm SSE. The chemical composition of the SEI film formed on Li metal was further investigated by an XPS experiment with depth profiling. Fig. S7† shows the XPS spectra of the Li1s, F1s and C1s elements. The Li1s spectra as shown in Fig. S7a† exhibit the following two assignable peaks: Li^0 at 55.0 eV and LiF at 57.1 eV.[29] The two peaks remained after 30 s, 60 s, 90 s and 120 s etching, while the intensity of the peak of Li^0 got enhanced with greater depth. The F1s spectra in Fig. S7b† show the following two assignable peaks: CF_3 at 691.5 eV and LiF at 687.5 eV.[30,31] The peak of LiF remained after 30 s, 60 s, 90 s and 120 s etching, which was consistent with the result of Li1s spectra, while the intensity of the CF_3 peak drastically descended after 30 s etching and disappeared after 60 s etching. The C1s spectra as shown in Fig. S7c† indicate the presence of species associated with C–C at 285.0 eV, C–N at 287.3 eV, C═O at 289.3 eV and CF_3 at 295.8 eV, respectively.[30,31] The peak of CF_3 disappeared after 30 s etching, which was consistent with the peak of CF_3 in F1s spectra, and the peak of C═O disappeared after 30 s etching. The two peaks of C–C and C–N remained after etching, while the intensity of the peak of C–C got enhanced with greater depth. The XPS results suggested that the formation of the SEI film was mainly attributed to the decomposition of the TFSI anions, as shown by the large presence of F compounds, while some C–N components could be attributed to both Pyr14 cations and TFSI anions.

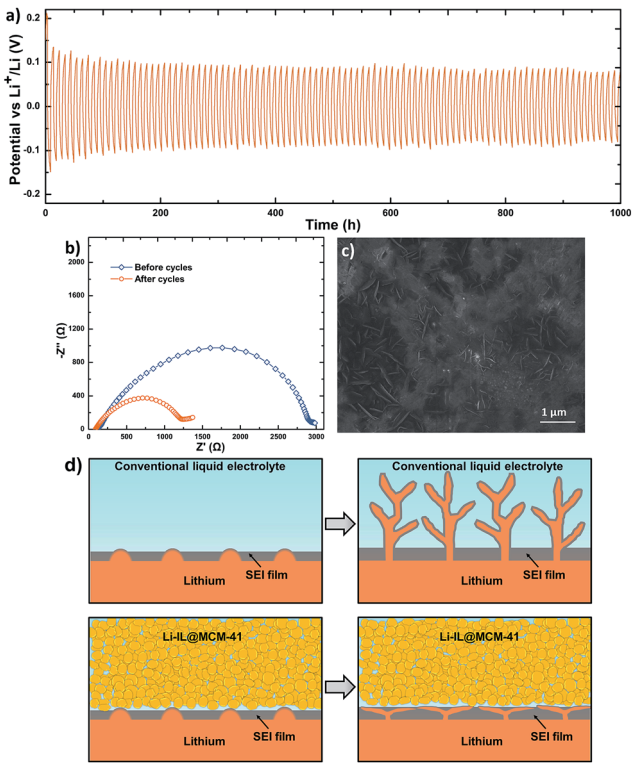

Fig. 3 (a) Voltage profile for the Li|Li-IL@MCM-41|Li symmetric cell at a current density of 0.025 mA cm^{-2}. (b) EIS of the Li|Li-IL@MCM-41|Li symmetric cell before and after Li plating/stripping cycles. (c) SEM morphology of the Li metal surface after Li plating/stripping cycles. (d) Schematic illustrations of the Li deposition process in conventional liquid electrolytes (upper panel) and the Li-IL@MCM-41 SSE (lower panel).

A unique solid-state battery system was designed and its architecture and working mechanism are illustrated in Scheme 1. The electroactive material was mixed with acetylene black and Li-IL@MCM-41 to form the solid-state composite cathode, and the mixture was pressed sequentially with an additional Li-IL@MCM-41 SSE into a double-layered structure as cathode/SSE layers. Li-IL@MCM-41 nanocomposites with plentiful nanowetted interfaces and acetylene black nanoparticles created a homogenously three-dimensional ion- and electron-conducting network, effectively connecting electroactive particles.

The battery performance of Li-IL@MCM-41 with different occupancy rates was firstly evaluated at 0.1C, using $LiFePO_4$ as the cathode material. As shown in Fig. S8,† Li-IL@MCM-41 with occupancy rates of 2.2, 2.0 and 1.7 mL@1 g delivered discharge capacities of 138, 105 and 87 mA h g^{-1}, respectively. As expected, the sample 2.2 mL@1 g delivered the largest discharge capacity because of its highest conductivity, and thus it was selected as the electrolyte, with $LiFePO_4$, $LiCoO_2$, and $LiNi_{0.8}Co_{0.1}Mn_{0.1}O_2$ as cathode materials to assemble solid-state batteries (SSBs), which were denoted as Li|Li-IL@MCM-41|LFP, Li|Li-IL@MCM-41|LCO and Li|Li-IL@MCM-41|NCM, respectively. The galvanostatic charge/discharge cycling performances of the three SSBs were evaluated at 0.1C (1C = 140, 140, and 200 mA g^{-1} for LFP, LCO, and NCM, respectively) rate at room temperature. As shown in Fig. 4a, an initial discharge capacity of 138 mA h g^{-1} for the Li|Li-IL@MCM-41|LFP SSB was recorded, and the reversible capacity was maintained at 138 mA h g^{-1} after 100 cycles. The Li|Li-IL@MCM-41|LCO SSB delivered an initial discharge capacity of 127 mA h g^{-1}, and the discharge capacity of 127 mA h g^{-1} can still be retained after 100 cycles as shown in Fig. S9a.† For the Li|Li-IL@MCM-41|NCM SSB, as shown in Fig. S9b,† an initial discharge capacity of 173 mA h g^{-1} was recorded, and its discharge capacity slightly decreased to 163 mA h g^{-1} after 100 cycles. For practical use, a Li|Li-IL@MCM-41|LFP SSB with higher active loading was also examined, as shown in Fig. S10,† and the capacity decreased a little due to the increased polarization. The above results demonstrated the excellent electrochemical stability of the Li-IL@MCM-41 SSE and its universal good compatibility with various electroactive materials. Such good battery performance can be ascribed to the efficient interfacial ionic conduction between electroactive grains and Li-IL@MCM-41 nanocomposites facilitated by the abundant nanowetted interfaces. From SEM and corresponding EDS images in Fig. S11,† the cathode layers and the electrolyte layers of the SSBs can be clearly distinguished without observable gaps, indicating the good contact between cathode and electrolyte layers. The specific energy and energy density of the Li|Li-IL@MCM-41|LFP SSB were calculated to be 105.0 W h kg^{-1} and 142.8 W h L^{-1} with optimized parameters (Table S1†), demonstrating its potential in practical applications. The battery performance and electrochemical properties of our Li-IL@MCM-41 SSE were also compared with the recently reported ones, as summarized in Table S2.†

The rate performance of the three SSBs was further evaluated at room temperature with the current rate increasing from 0.1 to 0.8C, as shown in Fig. 4. The discharge capacities of all three SSBs decreased as the discharge rates increased, which should be attributed to the increasing polarization as indicated by the charge–discharge profiles. Although the Li-IL@MCM-41 SSE

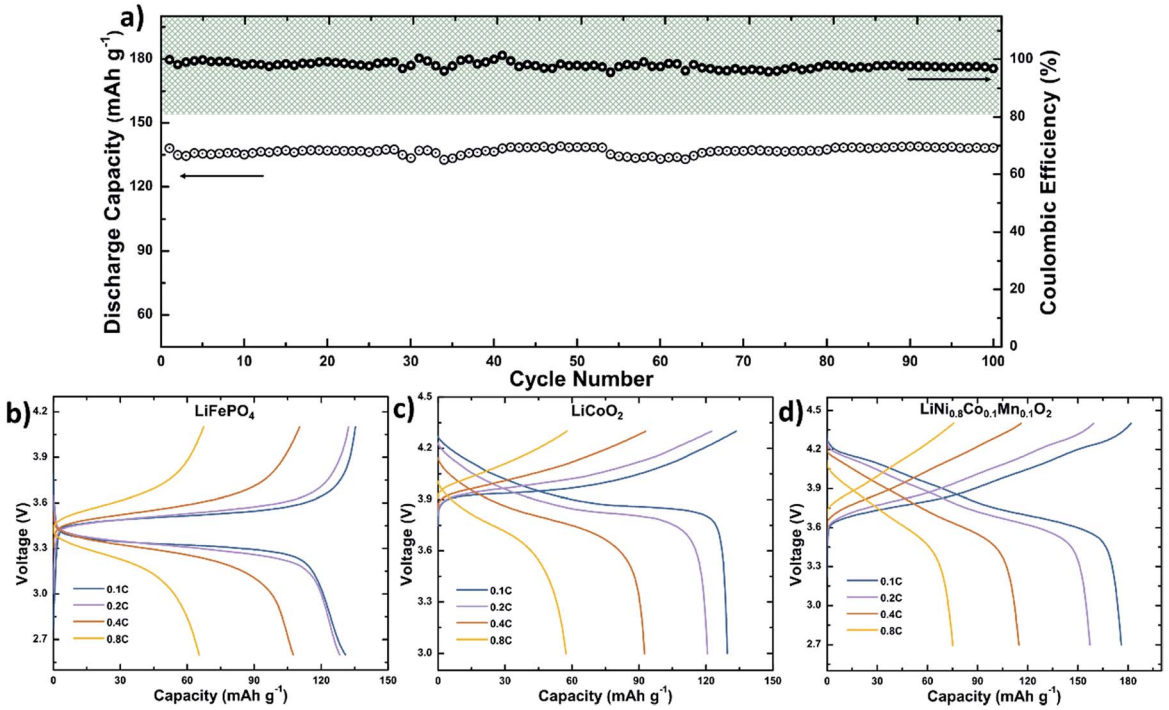

Fig. 4 (a) Cycling performance of the Li|Li-IL@MCM-41|LFP SSB at 0.1C rate at room temperature. Charge/discharge curves at different rates (0.1C, 0.2C, 0.4C, and 0.8C) at room temperature of (b) Li|Li-IL@MCM-41|LFP, (c) Li|Li-IL@MCM-41|LCO, and (d) Li|Li-IL@MCM-41|NCM SSBs.

possesses inferior conductivity to liquid electrolytes, the three SSBs exhibited acceptable rate performances at room temperature.

Conclusions

In summary, we prepared a solid-state electrolyte for lithium metal batteries by the nanoconfinement of Li-IL within the MCM-41 nanoporous scaffold. Featuring a high specific surface area with a large pore volume to confine enough Li-IL and plentiful nanowetted interfaces, the Li-IL@MCM-41 SSE exhibited a high ionic conductivity of 3.98×10^{-4} S cm^{-1} at 30 °C. It also possessed a broad electrochemical window and excellent thermal stability. The as-pressed SSE pellets, possessing sufficient mechanical strength, were demonstrated to suppress the dendritic deposition of the Li metal anode by direct SEM evidence. The solid-state batteries based on the Li-IL@MCM-41 SSE exhibited excellent cycling performance, and delivered capacities of 138 mA h g^{-1}, 127 mA h g^{-1}, and 163 mA h g^{-1} after 100 cycles at room temperature at 0.1C for $LiFePO_4$, $LiCoO_2$, and $LiNi_{0.8}Co_{0.1}Mn_{0.1}O_2$, respectively. The Li-IL@MCM-41 SSE was proved to establish efficient interfacial ion transport with different cathode materials and had a stable interface towards the lithium metal anode favoured by its nanowetted interfaces. This work has provided a promising approach to the design of novel solid-state electrolytes for lithium metal batteries.

Conflicts of interest

There are no conflicts to declare.

Acknowledgements

This work was financially supported by the National Key R&D Program of China (2016YFB0700600), National Natural Science Foundation of China (51672012), Shenzhen Science and Technology Research Grant (JCYJ20150729111733470, JCYJ20151015162256516), and China Postdoctoral Science Foundation (2017M620520).

References

1 D. Lin, Y. Liu and Y. Cui, *Nat. Nanotechnol.*, 2017, **12**, 194–206.
2 J. Lu, Z. Chen, F. Pan, Y. Cui and K. Amine, *Electrochem. Energy Rev.*, 2018, **1**, 35–53.
3 W. Xu, J. Wang, F. Ding, X. Chen, E. Nasybulin, Y. Zhang and J.-G. Zhang, *Energy Environ. Sci.*, 2014, **7**, 513–537.
4 M. D. Tikekar, S. Choudhury, Z. Tu and L. A. Archer, *Nat. Energy*, 2016, **1**, 16114.
5 R. Gao, R. Tan, L. Han, Y. Zhao, Z. Wang, L. Yang and F. Pan, *J. Mater. Chem. A*, 2017, **5**, 5273–5277.
6 A. Manthiram, X. Yu and S. Wang, *Nat. Rev. Mater.*, 2017, **2**, 16103.
7 B. Zhang, R. Tan, L. Yang, J. Zheng, K. Zhang, S. Mo, Z. Lin and F. Pan, *Energy Storage Mater.*, 2018, **10**, 139–159.
8 Y. Kato, S. Hori, T. Saito, K. Suzuki, M. Hirayama, A. Mitsui, M. Yonemura, H. Iba and R. Kanno, *Nat. Energy*, 2016, **1**, 16030.
9 Y. Tian, F. Ding, H. Zhong, C. Liu, Y.-B. He, J. Liu, X. Liu and Q. Xu, *Energy Storage Mater.*, 2018, **14**, 49–57.
10 W. Li, S. Zhang, B. Wang, S. Gu, D. Xu, J. Wang, C. Chen and Z. Wen, *ACS Appl. Mater. Interfaces*, 2018, **10**, 23874–23882.
11 J. Zhang, X. Zang, H. Wen, T. Dong, J. Chai, Y. Li, B. Chen, J. Zhao, S. Dong, J. Ma, L. Yue, Z. Liu, X. Guo, G. Cui and L. Chen, *J. Mater. Chem. A*, 2017, **5**, 4940–4948.
12 N. Chen, Y. Dai, Y. Xing, L. Wang, C. Guo, R. Chen, S. Guo and F. Wu, *Energy Environ. Sci.*, 2017, **10**, 1660–1667.
13 J. Zhang, Y. Bai, X.-G. Sun, Y. Li, B. Guo, J. Chen, G. M. Veith, D. K. Hensley, M. P. Paranthaman, J. B. Goodenough and S. Dai, *Nano Lett.*, 2015, **15**, 3398–3402.
14 M. Armand, F. Endres, D. R. MacFarlane, H. Ohno and B. Scrosati, *Nat. Mater.*, 2009, **8**, 621–629.
15 Z. Wang, R. Tan, H. Wang, Y. Luyi, J. Hu, H. Chen and F. Pan, *Adv. Mater.*, 2017, **30**, 1704436.
16 Z. Wang, Z. Wang, L. Yang, H. Wang, Y. Song, L. Han, K. Yang, J. Hu, H. Chen and F. Pan, *Nano Energy*, 2018, **49**, 580–587.
17 J. S. Beck, J. C. Vartuli, W. J. Roth, M. E. Leonowicz, C. T. Kresge, K. D. Schmitt, C. T. W. Chu, D. H. Olson, E. W. Sheppard, S. B. McCullen, J. B. Higgins and J. L. Schlenker, *J. Am. Chem. Soc.*, 1992, **114**, 10834–10843.
18 M. Nádherná, J. Reiter, J. Moškon and R. Dominko, *J. Power Sources*, 2011, **196**, 7700–7706.
19 C. Arbizzani, G. Gabrielli and M. Mastragostino, *J. Power Sources*, 2011, **196**, 4801–4805.
20 J.-H. Shin, P. Basak, J. B. Kerr and E. J. Cairns, *Electrochim. Acta*, 2008, **54**, 410–414.
21 R.-S. Kühnel, N. Böckenfeld, S. Passerini, M. Winter and A. Balducci, *Electrochim. Acta*, 2011, **56**, 4092–4099.
22 T. Frömling, M. Kunze, M. Schönhoff, J. Sundermeyer and B. Roling, *J. Phys. Chem. B*, 2008, **112**, 12985–12990.
23 S. Giri, B. G. Trewyn, M. P. Stellmaker and V. S.-Y. Lin, *Angew. Chem., Int. Ed.*, 2005, **44**, 5038–5044.
24 M. Choi, W. Heo, F. Kleitz and R. Ryoo, *Chem. Commun.*, 2003, 1340–1341.
25 Z. Wang, R. Tan, H. Wang, L. Yang, J. Hu, H. Chen and F. Pan, *Adv. Mater.*, 2017, **30**, 1704436.
26 S. Choudhury, R. Mangal, A. Agrawal and L. A. Archer, *Nat. Commun.*, 2015, **6**, 10101.
27 P. G. Bruce and C. A. Vincent, *J. Electroanal. Chem. Interfacial Electrochem.*, 1987, **225**, 1–17.
28 W. Liu, Y. Mi, Z. Weng, Y. Zhong, Z. Wu and H. Wang, *Chem. Sci.*, 2017, **8**, 4285–4291.
29 J. Zheng, X. Fan, G. Ji, H. Wang, S. Hou, K. C. DeMella, S. R. Raghavan, J. Wang, K. Xu and C. Wang, *Nano Energy*, 2018, **50**, 431–440.
30 J. Mun, T. Yim, J. H. Park, J. H. Ryu, S. Y. Lee, Y. G. Kim and S. M. Oh, *Sci. Rep.*, 2014, **4**, 5802.
31 S. Xiong, K. Xie, E. Blomberg, P. Jacobsson and A. Matic, *J. Power Sources*, 2014, **252**, 150–155.

